 doi:10.20944/preprints202105.0014.v1

Article

Investigation of the Time-Lapse Changes with the DAS Borehole Data at the Brady Geothermal Field Using Deconvolution Interferometry

Hilary Chang [1,†,*] and Nori Nakata [1,2,†]

[1] Massachusetts Institute of Technology, 77 Massachusetts Avenue, 54-216, Cambridge, MA, 02139, USA; nnkata@mit.edu,
[2] Lawrence Berkeley National Laboratory, CA 94720, USA
* Correspondence: hilarych@mit.edu
† These authors contributed equally to this work.

Abstract: The distributed acoustic sensing (DAS) has great potential for monitoring natural-resource reservoirs as well as borehole well-beings. However, the DAS wavefields of these applications are complicated and the noise levels are often high due to unknown coupling conditions. Therefore, we seek for an advanced array processing technique that takes advantages of the high spatial receiver density of DAS. In this study, we apply seismic interferometry based on deconvolution to DAS borehole data observed at the Brady geothermal field in Nevada to extract coherent and interpretable waves. The data is from the PoroTomo project at the Brady geothermal field in Nevada. With the deconvolution, we extract strong reverberating signals between 0-165 m depth due to the resonance of the borehole casing. We investigate the propagating velocity of the extracted waves and the velocity variation compared to depth, observation time, temperature, and pressure. With analytical and numerical modeling, we discover that a simple string model with multiple sources can explain the observed data well. The key to explain our observation is the sources coherency, and reflection coefficients at the boundaries. The amplitude spectra show clear normal modes of such reverberations, which are useful for dispersion analysis of the waves. For DASV below 200 m depth, we only obtain signals during the active seismic operation time due to poor coupling. Deconvolution interferometry is a powerful tool for analyzing the large volume of data observed by DAS and monitoring time-lapse changes of the propagation media and external sources.

Keywords: distributed acoustic sensing; borehole; time-lapse

1. Introduction

The distributed acoustic sensing (DAS) and distributed temperature sensor (DTS) have large potentials for applications in borehole environments, especially for geothermal reservoir monitoring. Applications of DAS in the borehole include flow monitoring [1–3], wellbore diagnostics [1,3,4], time-lapse structural monitoring with vertical seismic profiling [5–8], micro-seismicity detection [9], and long-period long-duration event detection for monitoring the response of hydraulic fracture [10]. Especially, the DAS is suitable for geothermal reservoirs monitoring for several reasons [11,12]: First, the DAS fiber has higher endurance in high temperature, high pressure, and corrosive environments compared to geophones. Second, the cost of DAS borehole deployment is relatively low, although the interrogator and the data storage can be expensive. Once installed, the fiber can be left in the well for long-term monitoring without changing locations, which are one of the main difficulties for conventional 4D (3D and time) surveys. Finally, the DAS provides very dense receiver arrays, although it is mostly 1D coverage. The DAS also has several challenges. The primary challenge is its lower signal-to-noise ratio (SNR), and good coupling is not trivial [9,13,14]. Secondly, the DAS data depend largely on

 doi:10.20944/preprints202105.0014.v1

cable design and layout of the survey and are less calibrated than geophones [12,14]. Hence, the DAS data requires more careful treatment. To deal with these challenges, we can use array processing techniques such as interferometry and stacking to extract signals from the data, taking advantage of the large number of receivers DAS provides to us.

In this study, we investigate the DAS data in a vertical borehole (DASV) from the PoroTomo Project at the Brady geothermal field, Nevada [15,16]. The PoroTomo project was a two-week experiment conducted during March 2016, during which the team conducted vibroseis experiments under varying operation intensities and collected a variety of geophysical data including surface DAS (DASH), borehole DAS (DASV), nodal geophones, InSAR, GPS, pressure, and temperature (DTS) data. With these rich data sets, Patterson *et al.* [17] and Patterson [18] analyzed the borehole DTS and pressure data to characterize the reservoir response at different stages of operations. Miller *et al.* [19] investigated the DASV data to find the signatures of earthquakes, vibroseis sweeps, and responses to the repetitive borehole processes. Trainor-Guitton *et al.* [20] migrated DASV active seismic data between 160-300 m depth and successfully imaged features on two nearby steeply dipping faults ($\sim$1 km away). However, these studies also point out the challenges of the Brady borehole DASV data. First, the SNR is low as the DASV cable is coupled to the wall of the borehole only through friction. Although Hartog [11] suggested frictional coupling provides sufficient SNR for deviated wells, the coupling of the Brady DASV cable seems to be poor because the well is vertical. Moreover, the lower part of DASV occasionally observed the slip of cables [19]. Second, the wavefield of the DASV data is complicated as multiple events caused by different phenomena interfere with each other, such as slips of the cable, ringing of the steel casing, vibroseismic sweeps, reflections [20], earthquakes signals, and disturbances due to borehole processes [19]. Our motivation, therefore, is to extract useful and interpretable signals from these complex wavefields.

We use deconvolution interferometry to extract signals from the DASV borehole data. This deconvolution method has been used in many previous studies. Nakata and Snieder [21] used surface and borehole sensors to monitored monthly and annually shear wave velocity changes at the near-surface; while Sawazaki *et al.* [22], Yamada *et al.* [23], and Bonilla *et al.* [24] analyzed this velocity changes during earthquake strong ground motion. Snieder and Safak [25] and Nakata *et al.* [26] extracted the vibration modes of a building during earthquakes using receivers on the building floors. Tonegawa *et al.* [27] reconstructed body waves from teleseismic earthquakes data and used them to image the Philippine slab. We can extract coherent waves along receivers with this deconvolution, which are governed by the same wave physics (i.e., wave equation) as original observed data. After extracting the signals, we analyze them to estimate propagating velocities and the velocity variations over time. In addition to velocity, the pattern of the signal in the deconvoluted wavefields and its variations can also reveal the source conditions [26].

In this paper, we first introduce the Brady DASV data and show the signals we obtain after applying deconvolution interferometry. We interpret the deconvolved wavefields above and below 200 m depth separately, since characterization of waves changes at this depth. Then, we focus on analyzing the reverberating signals above 200 m depth. We estimate the velocity and its variations versus frequencies, depth, time, temperature, and pressure. Finally, we analytically and numerically model the observed wavefields using a simple string model with multiple sources.

2. Data

We focus on the DASV, the DTS temperature, and the pressure data from the PoroTomo project [15,16]. The DASV and DTS fibers are co-located in one borehole (red star in Figure 1; well 56-1) and the pressure sensor is located at a nearby well (green cross in Figure 1; well 56A-1). The DASV and DTS cables are nearly 400 m long in the well. The DASV system has 384 channels (i.e., stations) with approximately 1 m channel

Preprints (www.preprints.org) | NOT PEER-REVIEWED | Posted: 3 May 2021 doi:10.20944/preprints202105.0014.v1

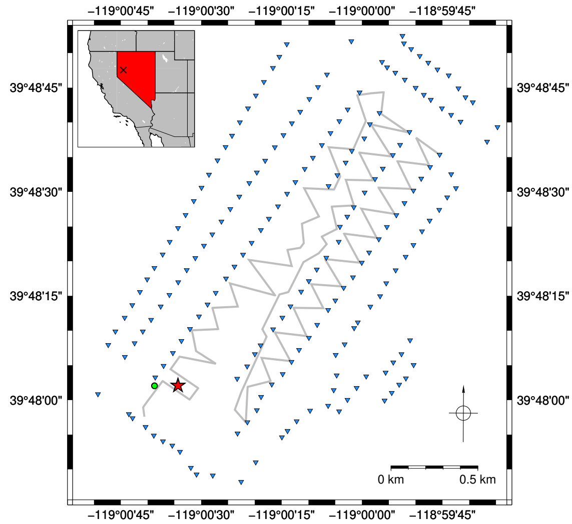

Figure 1. Configuration of the PoroTomo experiment. The survey was at the Brady geothermal field in Nevada, USA (black cross in the inset). The red star is the borehole (well 56-1) with DASV and DTS. The green dot is the borehole (well 56A-1) with the pressure sensor. The blue triangles are the locations of the vibroseis shots. The grey lines are the DASH cable on the surface. We use DASV, DTS, and pressure data in this study.

spacing. The ground is about 1230 m above sea level near well 56-1 and 56A-1. The DASV fiber is single-mode and the DTS fibre is multi-mode, both are high temperature acrylate-coated, which is tested to be resilient up to 150°C. The cable is protected by 316 stainless steel double tubing. The DASV system has a gauge length of 10 m with sampling rate of 1000/s. Since DAS measures the average optical phase change across the gauge length, the unit of the observed data is radian/millisecond/gauge length. The total DASV data size is 981 GB stored in SEG-Y format. The DTS system has channel interval of 0.126 m and sampling interval of 62 s. The pressure sensor is at an elevation corresponding to channel 219 of the DASV system (i.e. measured depth = 219 m). The sampling interval of the pressure sensor is 60 s. The two wells are around 100 m away from each other; they were hydraulically connected suggested by Patterson [18] based on simultaneous responses between the DTS and the pressure sensor.

Measurements of DASV, DTS, and pressure were continuous in time and overlapped for about eight days (Figure 2). The pressure was observed in longer time. The analysis period starts with a drastic pressure drop during 3/18 due to increased operation after a long shutdown period. Then, the pressure increases slowly due to increasing injection until resuming to normal operation on 3/24. The pressure bump at the end of 3/25 is due to an unplanned plant shutdown [28]. The temperature profile increases with depth in general with a heat deficit below 320 m due to historical geothermal explorations in this region [19]. The temperature was lower initially in early 3/18 because the well was cooled with water before cable installation for safety reason. The temperature raised back slowly with time and reached its high of around 160°C at the depth of ∼260 m. The maximum temperature is around 160 °C. The DASV DC and RMS amplitudes are calculated with 30 mins time window with 50% overlap.

We note some features that have been investigated in previous studies. On 3/18-3/19, the depressurization processes following the pressure drop caused the steam/water interface to move downward from 115 to 120 m, suggested by Patterson *et al.* [17] and Miller *et al.* [19] based on the trend of the temperature transitions (Figure 2b). During this time, the DC levels on the upper part of DASV were high (Figure 2c). In addition to the interface of the steam/water boundary at ∼120 m, the casing structure and fluid exchanges also affect the data. The first casing ends at 90 m, below which is the second well casing down to 310 m. Below 310 m is the zone with high permeability, and all the

Preprints (www.preprints.org) | NOT PEER-REVIEWED | Posted: 3 May 2021 doi:10.20944/preprints202105.0014.v1

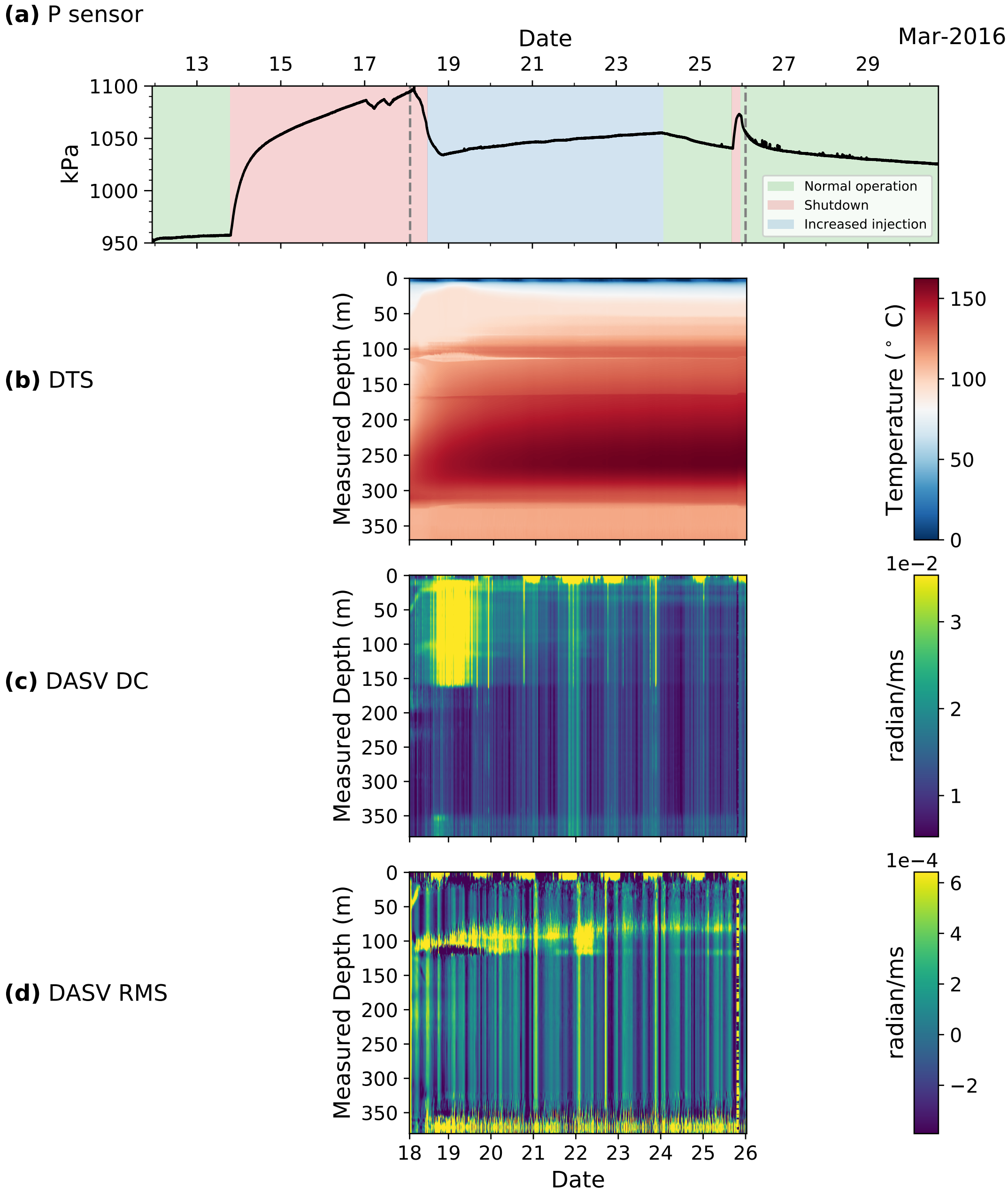

Figure 2. (**a**) Pressure and corresponding field operation stages [28], (**b**) DTS temperature, (**b**) DASV DC amplitude, and (**d**) DASV root-mean-square (RMS) amplitudes of non-filtered observed data aligned in time. The analysis period of this study is 3/18-3/25 (eight days; marked by gray dashed lines), when we have all pressure, DTS, and DASV data simultaneously. The DC and RMS amplitudes are calculated with 30 mins time window with 50% overlap.

borehole has no casing [17]. We anticipate that the high RMS amplitudes below 350 m would related to the fluid exchange between inside and outside boreholes. Patterson *et al.* [17] observed advection possibly due to fluid movement at 165 m, where casing might have a problem such as cracks or poor coupling. This weak spot likely causes the division between the upper and lower DASV, which is noticeable in Figure 2c and will be more pronounced in the deconvolved wavefields in the following sections. The surface diurnal cycles in Figure 2b-d are related to daily variations of temperature and noise level.

3. Methods and analysis results

3.1. Extraction of coherent waves

3.1.1. Review of deconvolution interferometry

The deconvolution interferometry deconvolves observed data at a reference channel (i.e., virtual-source channel; Wapenaar *et al.* [29]) with the rest of the channels and stacks the resulting deconvolved wavefields over time to improve SNR. The deconvoluted wavefield D in the frequency domain is given by [26]:

$$D(z, z_a, \omega) = \frac{U_z(\omega)}{U_{z_a}(\omega)} \tag{1}$$

$$\approx \frac{U_z(\omega)U^*_{z_a}(\omega)}{|U_{z_a}|^2 + \epsilon\langle|U_{z_a}|^2\rangle} \quad , \tag{2}$$

where z is the depth of each channel, z_a is the depth of the virtual source channel, and ω is the angular frequency. The deconvolution operation in the frequency domain is the division of the wavefields of channels at each depth ($U_z(\omega)$) by the wavefield at the depth of the virtual source ($U_{z_a}(\omega)$). The symbol * denotes the complex conjugate. Equation 2 is for stability of the operator, and we use $\epsilon = 0.5\%$ to scale the average power spectrum ($\langle|U_{z_a}|^2\rangle$) in the denominator to avoid zero-division.

To improve SNR of the deconvolved wavefields [30] and also enhance the temporal resolution of time-lapse measurements, we use three types of time intervals for the processing. The time window of each trace for one correlogram (t_{win}), the time step to slide the time window and calculate the next correlogram (t_{step}), and the time span that we stack all the correlograms within it and get a stacked correlogram (t_{span}). Note that the length of these time intervals relates to the computational cost. A proper t_{win} has to include the duration of the target signals at its minimum. A shorter t_{step} or longer t_{span} increases stack number and improve SNR. An interval being too long loses the resolution in time and increases the computational cost. We use two sets of these time intervals in this study. For the purpose of tracking the velocity of the strong signals on the upper part of DASV (Section 3.2), we use $t_{win} = 1$ mins, $t_{step} = 0.5$ mins, and $t_{span} = 1$ hrs. The SNR of the reverberating signals in the upper part is good using this short time interval. For the purpose of observing the wavefield patterns and getting weak signals (Section 3.1.2 and Appendix A, we use $t_{win} = 30$ mins, $t_{step} = 15$ mins, and $t_{span} = 3$ hrs. These longer time intervals are required for enhancing the SNR in the lower part. Before converting the data to the frequency domain for deconvolution, we demean, detrend, and taper (10% on both sides) the raw data in the time window (t_{win}).

3.1.2. Deconvolved wavefields

We compute deconvolution between all pairs of receivers. The deconvoluted wavefields are distinctly different between the upper and lower parts of the borehole. The upper part between 10-165 m is dominated by strong reverberating signals and between 165-200 m is a transition zone (Figure 3). The lower part is below 200 m that contains weak signals and no reverberation (Figure A1).

We focus on the consistent signal on the upper part and analyze its temporal variations. We discuss the extracted signals in the lower part in Appendix A.

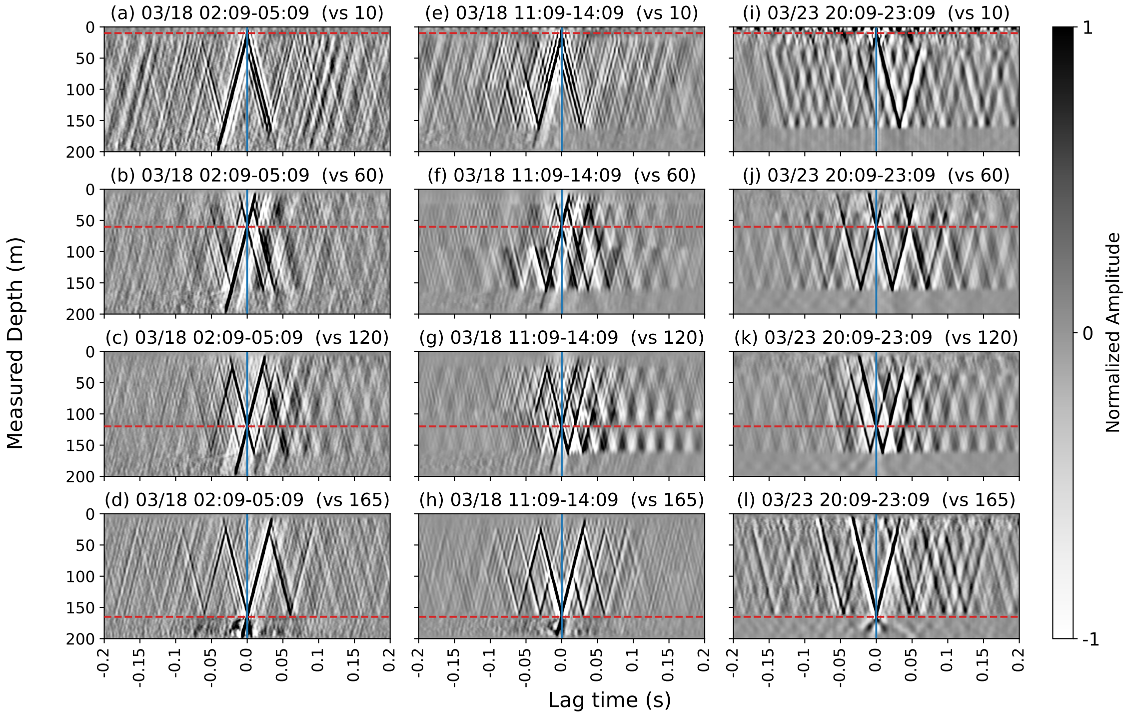

Figure 3. The DASV stacked deconvolved wavefields between measure depth 0-200 m at three example times (as three columns) using four different virtual sources channels (as four rows). They are calculated using deconvolution interferometry with $t_{win} = 30$ mins, $t_{step} = 15$ mins, and $t_{span} = 3$ hrs. The time in each subplot indicates the 3-hour stacking period. The vs shows the measured depth of the virtual source channels (the red dashed lines). The blue vertical lines mark the zero-lag of the correlograms.

The reverberations between 10-165 m always present during the eight days of the analysis period (Figure 3). Moving the virtual source along this depth range, the direct-wave patterns change and different sets of multiples (that have different time shifts between them) move inward and outward simultaneously in both causal and acausal sides of the correlograms. Although the direct waves and the multiples overlap each other that makes the wavefield complicated, deconvolution makes waves interpretable and these waves are useful for estimating propagation velocity of the wave. At 165 m, the wavefields have an abrupt change, below which we do not see the reverberations. The depth of this abrupt change corresponds to the depth of the advection activities observed in Patterson *et al.* [17] and is interpreted as resulting from as a defect on the casing. This depth behaves as a reflector of these waves. When the virtual source is at the transition zone between 165-200 m, we see strong up-going waves during 3/18-3/19 which means this depth range contains the source for the upper reverberations during this time.

At different time and date (across the columns in Figure 3), the patterns of the wavefields remain similar to each other, but the frequency contents and noise levels change according to external source conditions as discussed below. To understand these wavefield patterns, we analyze the temporal variations of velocity of this signal in Section 3.2 and the source conditions that generate these patterns in Section 4 and Appendix B.

3.2. Time-lapse changes of wave velocities

To understand the reverberating signal between 10-165 m which consistently appears over the entire analysis period and the medium it propagates in, we analyze wave velocities and their time-lapse changes. Every one hour of ambient-noise data, we can extract coherent traveling waves, and hence we use them to estimate accurate velocities at each hour. We measure the arrival time of first up-going waves at each channel by picking the peak of the first arrivals in the deconvolved wavefields. The slopes of the picked arrival times provide the velocities. We focus on channels between 70-120 m, where the signal appears consistently over the eight days and shows the highest SNR. We only use the phase parts for our interpretation and do not use the amplitudes, because the amplitudes of the deconvolved waves extracted from ambient noise are complicated to interpret [31]. The modeling shown in Appendix B will help understanding the amplitudes. The measured velocities against measured depth, time, temperature, and pressure are plotted in Figure 4. We estimate the velocity variations of each channel that spaces 1 m between each other at the depth range 70-120 m (Figure 4a). The channels at shallower depth has a higher mean velocity (∼4400 m/s) than the channels at deeper depth (∼4100 m/s). Between 95-105 m depth near a change of casing diameter, the velocities vary at a wider range. The mean velocity shows a sudden rise from 4100 to 4700 m/s in early 3/18 (the black curve in Figure 4b), falls back to 4100 m/s before late 3/19, and fluctuates between 4100-4300 m/s for the remaining of the analysis period. The initial fall back occurs simultaneously for all target channels but the fluctuations afterward vary among individual channels. The velocity decreases with increasing temperature with a slope of -17.1 m/s/°C (Figure 4c). We do not observe obvious correlation between velocity and pressure except very low pressure zones (Figure 4d) because of the lack of samples at higher pressure.

3.3. Normal-mode analysis

The deconvoluted wavefield of a vibrating 1D structure can be written as the summation of normal-mode [25,26]. Figure 5 shows the amplitude spectrum of deconvolved wavefields with the virtual source at 180 m calculated using one minute time window and stacked over one hour. The normal-modes of the signal are clearly decomposed between 10-165 m. The system has closed boundary on both sides (top and bottom) of wave propagation, which makes sense for P-wave propagation. The frequency interval between different modes is about 18 Hz and consistent over all modes as expected. The first mode is, based on the shape of the spectrum, at around 20 Hz, but its amplitude is small. The second and higher modes are stronger.

We observe that the mode frequency and the system length (H) are changing during the analysis period. The change in the system length may be caused by the variation of boundary conditions and/or coupling. This implies that the phase velocity c perturbs, as we found in Figure 4. For the system with closed boundaries, the phase velocities at each mode m are represented as

$$c_m = \frac{2 f_m H}{m} \quad , \tag{3}$$

where f_m is the mode frequency, H is the spatial length where the signal propagate. We estimate the velocity changes using Equation 3 focusing on the 2nd (∼38 Hz), the 3rd (∼55 Hz), and the 4th (∼71 Hz) modes, since these three modes are the most significant. We extract f_m by picking the largest peaks in frequency for these three modes in the hourly stacked amplitude spectrum at 6 or 7 am on each day, which is the time that has relatively high SNR. We estimate H by measuring the length of the DAS segment in which the mode present (i.e., the depth difference between the upper and lower boundaries where the amplitudes reduce to background level).

Preprints (www.preprints.org) | NOT PEER-REVIEWED | Posted: 3 May 2021 doi:10.20944/preprints202105.0014.v1

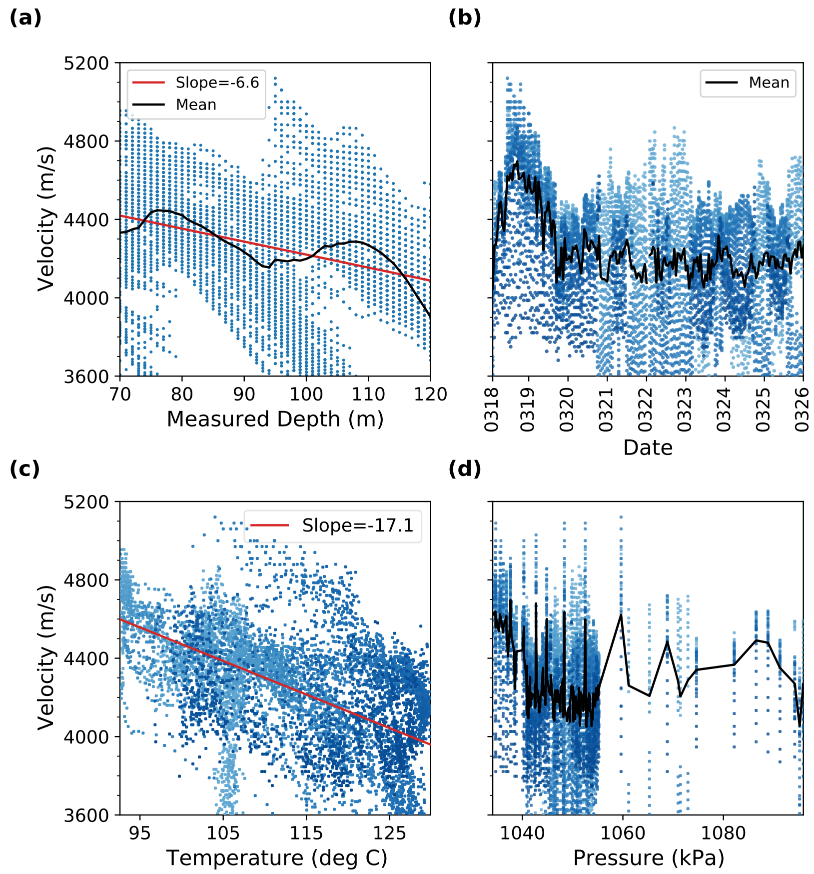

Figure 4. The velocity of the signal between 70-120 m versus (**a**) depth, (**b**) time, (**c**) temperature, and (**d**) pressure. The velocities are calculated by measuring the slope of the the first arrivals on the causal side of the hourly deconvolved correlogram. Each blue dot is a velocity measurement at one channel. In (**b**)-(**d**), measurements from deeper channels are distinguished by gradually darker blue colors. The red line in (**c**) shows the trend of the linear fit. The black curves in (**a**), (**b**), and (**d**) show the average velocity.

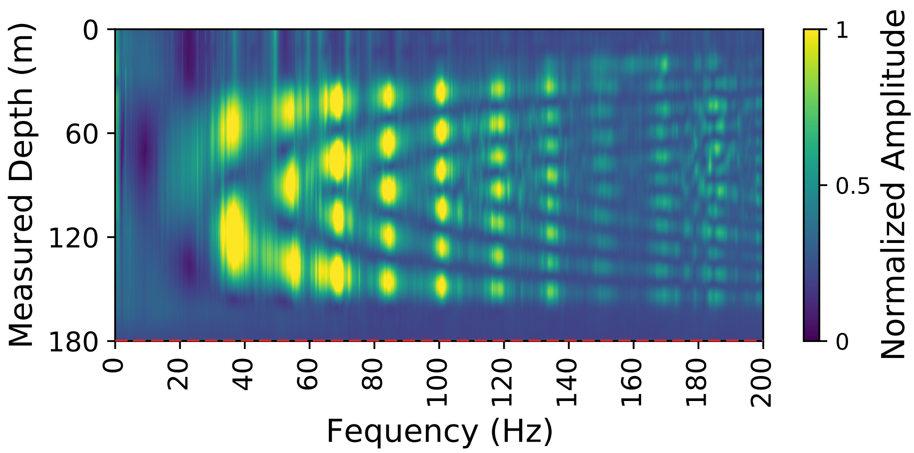

Figure 5. The deconvolved magnitude spectrum of DASV between 0-180 m on 3/18 6 am (using one minute time window, stacked over one hour). The spectrum shows that the reverberating signal between this depth range can be decomposed into normal-modes. The red dashed line marks the virtual source at 180 m.

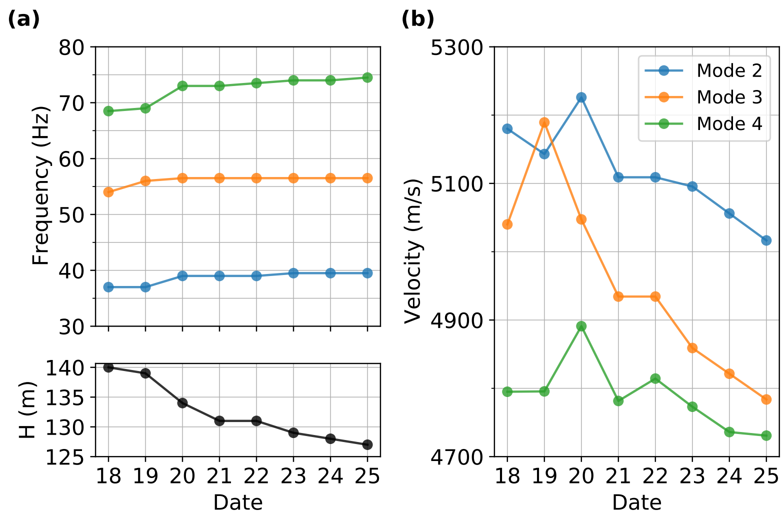

Figure 6. (**a**) The peak frequencies and the length of segment where the signal is present (H) that are picked from the 2nd, the 3rd, and the 4th modes in the stacked deconvolved spectrum (e.g., Figure 5). The peak frequencies increase with time; whereas the length decreases mainly resulted from the top end of the signal getting deeper by 13 m at the end of the analysis period. (**b**) The phase velocities of the signals derived from Equation 3 show a general decreasing trend versus time.

In Figure 6a, the mode frequencies get slightly higher while the length where the signal propagates gets shorter. The top boundary drops about 13 m, which is likely related to large temperature decreases at shallow depth between 10-40 m, while the bottom point of reflection does not shift significantly. Figure 6b is the velocities calculated using Equation 3. The velocities estimated using higher modes are lower, suggested a negative frequency-velocity dependency, and hence the velocities are dispersive. In general, all of the three modes show similar trends; the velocities increase for the first few days before 3/20, and then, they continuously decrease until the end.

4. Discussions

4.1. Signals on the upper part

As Miller *et al.* [19] suggested, the reverberation is mainly due to the resonance of the production-well casing, which is possibly caused by losing cement behind the casing above 165 m depth. If the well casing was well-bonded to the cement, the reverberation would be damped in a few tens of microseconds [32]. This indicates that reverberations we extract using deconvolution interferometry can be used to monitor the casing conditions in space and time. The shaking of the DASV steel cable jacket might also contribute to this signal, but the contribution is neglegible since the direct waves disappear when we put the virtual source at below 200 m. If the vibration of the cable jacket is a dominant signal, we expect to see direct waves emitted from virtual sources across the entire cable after deconvolution. Compared with the weak signals in the lower part of the borehole, the casing resonance on the upper part is stronger and masks any potential energy from the formation. Nevertheless, we can still obtain information about the integrity of the casing and energy sources by analyzing this resonance for the upper part.

The reverberating signal behaves like the vibrating response of a building to earthquakes [25,26]. The velocity estimated from traveling waves and normal-modes are close to the longitudinal wave speed of steel rods (5000-5250 m/s; Haynes [33]) for both up-going and down-going waves, which are significantly higher than those in the local formation (V_p=1000-2500 m/s in Parker *et al.* [34], Thurber *et al.* [35]). Therefore, we conclude that the extracted waves propagate in the steel casing as compressional waves, and they are sensitive to casing, coupling of casing to the ground, and fluid in the borehole [36]. Comparing the velocities estimated by the two methods, the normal-mode method yields slightly higher velocities than the traveling wave method. This is because the normal-mode analysis is done on the lower frequency modes that have higher velocities (Figure 6b) whereas the traveling waves contain all frequencies. The frequency-dependent velocities from the normal-mode analysis are useful to obtain attenuation and structures at different distance from the well. However, the coupling between casing and the formation was poor as discussed below. Hence, the negative frequency-velocity relation might be caused by the casing and fluid in the borehole, but we need a further experiment to understand the dispersion of the waves.

The velocity increases when temperature decreases (Figure 4c). The mean dV/dT relation (-17.1 m/s/°C) is much higher than that measured in the lab for pure steel material using an ultrasonic method (-0.5 m/s/°C, Mott [37], Droney *et al.* [38]). This is because the casing materials are not pure steel [19]. Instead, they are Oil Country Tubular Goods (OCTG) graded alloy steel for higher hardness and corrosion resistance. Thus, we find this non-pure steel has higher sensitivity to the temperature. In Figure 4a, the negative depth-velocity trend reflects the temperature-velocity dependency since temperature increases with depth at this depth range (Figure 2b). The depth-velocity plot has a wider velocities spread near 95-105 m which is likely related to complicated signal due to change of casing structure at the depth. As for the temporal variation in Figure 4b, the high velocity during 3/18-3/19 is associated with the depressurization processes in the borehole due to the initial pressure drop, which also corresponds to the time of the high DC level at the upper part of the borehole (Figure 2c).

The shape of the wavefield and its reverberation in Figure 3 contain information of noise sources and the reflectivity at the boundaries. According to Nakata and Snieder [31], to have the symmetry between causal and acausal time as seen in Figure 3, we must have more than one sources. Based on the numerical simulation in Appendix B, the two major sources at the top and bottom of the upper part enclosing this depth range are able to produce the main direct-wave and multiple patterns in Figure 3. These observed deconvolved waves are emitted from the virtual source at time equals to 0 s, which requires the two major sources being uncorrelated; otherwise, we would expect to have excitation of waves at the correlated source location at the zero-lag time (Appendix B.3). We suspect that the source from below is associated with a potential weak spot on the casing at 165 m, where we likely have fluid advection between the internal of the borehole and the formation [18,19]. This spot also behaves as a physical reflector to general reverberations because the waves are difficult to propagate through. The source from above is associated with surface operations and anthropogenic noises. Because the relative intensity of the sources changes over the analysis period, the patterns of deconvolved signals perturb over the time (Figure 3). The amplitude of the multiples get smaller in later times in both causal and acausal axes, which agrees with the simulation in Appendix B.4. To produce the strong multiples in the data, we estimate the reflection coefficient should be at least higher than 0.5 for the top and bottom reflectors.

In addition to the major multiples, many smaller-amplitude multiples with different time shifts also present in the deconvolved wavefields (Figure 3). As the virtual source moves along the cable, the location of these small multiples changes as well; some of the multiples move toward zero-lag while some of them move outward. This indicates that the sources for these small multiples are in the system between 10-165 m. The direct waves of these smaller sources emit simultaneously with the major direct waves, which suggests that they are mutually correlated, as the simulation in Appendix B.5 shows. Potential origins of these smaller sources are weak spots and/or fractures in this depth range, as expected from the source locations for the major sources at the top and bottom of the upper part [18,19]. Nakata and Snieder [31] simulated distributed sources between two reflectors. Although their simulated wavefields only have one direct wave, due to the sources being uncorrelated. In our case, we have both uncorrelated major sources and correlated smaller distributed sources, which makes that we have one strong waves excited at the virtual source location and many small events that also propagates with medium velocities.

We now interpret the wavefield patterns shown in Figure 3. Figure 3a-d show the extracted wavefields on 3/18 during which a drastic pressure drop occurred due to increased field operation after a shutdown period. When the virtual source is at the transition zone between 165-200 m, we have much stronger direct waves on the causal side than on the acausal side, which indicates a dominant source located in between this depth range or below. As the virtual source moves up to above 165 m, the acausal direct wave shows up as well as the multiples since we are inside of the reflectors that enclose the resonance. The multiples begin to overlap as we move further away from the dominant source between 165-200 m. When the virtual source is at 10 m depth, the multiples converge to a single reversed V centered at the zero-lag time, as similar to the earthquake deconvolution studies [25]. These behaviours are similar to the simulation in Figure B2a where we have a strong bottom source. Figure 3e-h are the extracted wavefields on 3/18 during the pressure drop. The apparent reflector at 90 m corresponds to a location where the casing diameter changes. This reflector can be a third source based on its similarity compared with Figure B5, but we do not have clear explanation of the origin of this source. This feature is the most obvious on 3/18 where there were large disturbances in the borehole but became weaker in later days. Figure 3i-l are the extracted wavefields on 3/23 during which a vibroseis truck was operating at some of the closest sites (around 100-600 m away). The top reflector seems to move from 10 to 35 m at this stage (Figure 6a). In Figure 3i, the direct wave is much more stronger on the causal side than on the acausal side, which indicates a dominant source from the surface. The pattern looks similar to Figure B2c where $|S_1|/|S_2| = 10$. As we move the virtual source downward below 35 m, the direct waves become more symmetric on the causal and acausal sides because we are inside of the resonance depth range. The apparent time shift between multiples of this direct wave is the largest when $vs = 35$ m and decreases as we move the virtual source further away from the surface, and finally, to 0 when the virtual source is at the boundary at the bottom.

4.2. Signals on the lower part

The signals we obtain on the lower part of the borehole are from the energies of different types of waves in the vibroseis experiment (Appendix A). Signals that are from outside of the borehole propagate through the formation and are sensitive to the mechanical properties changes in the formation. However, due to poor SNR on the lower part of the borehole, it is difficult to analyze the velocity variation with satisfying precision. The poor SNR is due to poor coupling between the cable and casing as the cable slipped during the rewarming [19]. If the coupling was better, the SNR would be improved and we could have signals outside of the vibroseismic experiment times. We can potentially apply the similar time-lapse velocity analysis as the upper part and infer for the changes of mechanical properties in the formation.

5. Conclusion

We demonstrate that deconvolution interferometry can extract time-lapse velocity changes of a system and help to understand the physical sources and boundary of the system. The deconvoluted wavefields calculated from Brady DASV borehole data have strong reverberations at the upper part of the borehole due to the resonance of the well casing. The steel casing is the main medium of the compressional wave propagation for this resonance. By investigating this reverberation, we obtain information regarding the integrity of the well casing, seismic sources, and time-lapse changes of well structure. Although the hourly deconvolved wavefields vary according to actual source intensities inside and outside borehole, we have enough repeatability of the waves to measure accurate velocities. We find that the propagating waves are sensitive to the perturbation of the alloy steel casing according to temperature, as the wave velocity decreases at higher temperature. The increase in velocity during the period of depressurization processes suggests that the intensity of the vibration gets higher during large disturbances in the borehole. The normal-mode analysis allows us to estimate frequency-dependent velocities. The extracted wavefields show dominant sources from surface vibroseismic operations and borehole processes, and suggest the existence of multiple sources along the upper part of the borehole, which reveals potentially weak casing cement bonding spots and/or fracture locations. Based on the numerical modeling of the wavefields, the reflectivity of the boundaries at the top and bottom of the upper part of the borehole is rigid, and the coefficient is larger than 0.5. For the lower part of the borehole, we only obtain coherent signals during vibroseismic operations. The SNR is low due to poor coupling which prevents us from estimating temporal or spatial velocity changes with acceptable precision. The technique proposed here can be applied to many different borehole DAS applications to diagnose the condition of casing structure, understand borehole processes, and estimate the properties of the reservoir. Furthermore, we can monitor time-lapse changes with continuous data.

Author Contributions: Conceptualization, H.C. and N.N.; methodology, H.C. and N.N.; software, H.C.; validation, H.C.; formal analysis, H.C.; investigation, H.C.; resources, N.N.; data curation, H.C.; writing—original draft preparation, H.C.; writing—review and editing, N.N.; visualization, H.C.; supervision, N.N.; project administration, N.N.; funding acquisition, N.N. All authors have read and agreed to the published version of the manuscript.

Funding: This study is supported by Japan Oil, Gas and Metals National Corporation and MIT-Indonesia seed funds.

Data Availability Statement: Publicly available data sets were analyzed in this study. This data can be found at the DOE Geothermal Data Registry (GDR) https://gdr.openei.org/

Acknowledgments: We appreciate the advice from Douglas Miller on DAS data processing; this study has benefited from several discussions with him. We also appreciate the comments from Michal Chamarczuk that helped improve the manuscript.

Conflicts of Interest: The authors declare no conflict of interest.

Abbreviations

The following abbreviations are used in this manuscript:

DAS	Distributed acoustic sensing
SNR	Signal-to-noise ratio
RMS	Root-mean-square

Appendix A Deconvolved wavefields at the lower part

As discussed in Section 3.1 and 4, the energy of reverberations in the upper part are very weakly observed below 165 m. Thus, almost no energy is propagating downward from this depth. We can obtain clear coherent waves only when vibroseis truck is active and demonstrate here the extracted waves. These waves have been used, without deconvolution analysis, to image subsurface structure [20].

We extract clear coherent waves from three-hour stacked deconvolved wavefields between 165-300 m during the time when the vibroseis truck was operating 100-600 m away (Figure A1). These waves propagate in different velocities. The first two signals travel downward with apparent velocity of 2100 m/s (green dashed lines) and 1100 m/s (pink dashed line). They are the direct P and S waves excited by the vibroseis truck. The V_p/V_s ratio is 1.91 which is consistent for shallow formations in Brady including volcanic sediments, limestone, lacustrine sediments, and geothermal features such as carbonate tufa [39]. The third signal has apparent velocity of 1400 m/s (the yellow dash line) and propagates upward, although it is weak. These waves can be a refletion from

Preprints (www.preprints.org) | NOT PEER-REVIEWED | Posted: 3 May 2021 doi:10.20944/preprints202105.0014.v1

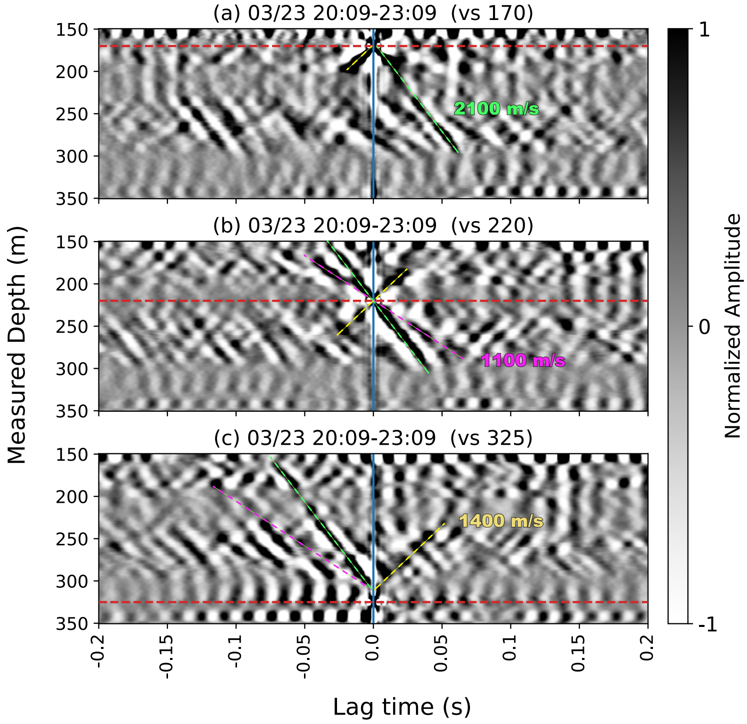

Figure A1. The DASV stacked deconvolved wavefields between measured depth 150-350 m during the time where a vibroseis truck was operating at nearby sites (100-600 m away). Three sets of signals are obtained using virtual sources at (**a**) 170 m, (**b**) 220 m, and (**c**) 325 m. The two down-going waves marked by the green and magenta dashed lines have apparent velocity of 2100 m/s and 1100 m/s, respectively. The up-going waves marked by the yellow dashed lines have apparent velocity of 1400 m/s.

nearby faults Trainor-Guitton *et al.* [20], Siler and Faulds [39], but the data are limited to identify the reflection point. Notice that using the channel below 300 m as virtual source, the waves still start at 300 m as shown in Figure A1c. The deconvolved waves below 300 m in Figures A1a,b are also less coherent and in phase between 300-360 m. The known change of the borehole casing would cause this change in deconvolved waves below 300 m, where the top of the slotted liner is at 296 m and the production casing ends at 302 m.

Appendix B Modeling deconvolved waves

Appendix B.1 Mathematical notation of wavefields

To explain the observed deconvolved wavefields (Figure 3), we use a simple string model following Nakata *et al.* [26] to analyze the observed deconvolved wavefield. The deconvolved wavefields from the field data in Figure 3 have several noticeable characters. The wavefields have strong waves in both causal and acausal waves, which are not expected from only the incoming waves from the bottom of the array [26]. Direct and reverberations are observed from the virtual source, and wavefields become complicated when we use receivers in the middle of the array as a virtual source. Also, the frequency content and wave complexities change over the time. Because the single source does not explain the observed data [31], we put two sources at the top and bottom of the system (Figure B1). This model can also represent the case when we have sources deeper [21]. In this case, we consider S_2 indicates the incoming wave from the bottom to the system.

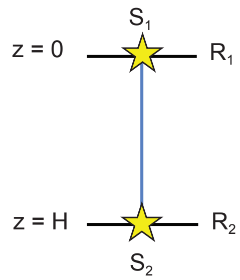

Figure B1. A simple 1D string model bounded by two reflectors at $z = 0$ (R_1) and $z = H$ (R_2) and a line of receivers (blue line) between them. The two sources are located at $z = 0$ (S_1) and $z = H$ (S_2) (yellow stars).

Nakata *et al.* [26] expressed the wavefield of a single source as the sum of a power series. Following their results, the wavefields of the two sources in Figure B1 are the superposition of their individual wavefields:

$$U(z,\omega) = \frac{S_1(\omega)(e^{z(ik-\gamma|k|)} + R_2 e^{(2H-z)(ik-\gamma|k|)}) + S_2(\omega)(e^{(H-z)(ik-\gamma|k|)} + R_1 e^{(H+z)(ik-\gamma|k|)})}{1 - R_1 R_2 e^{2H(ik-\gamma|k|)}}, \quad \text{(B1)}$$

where z is depth, ω is the angular frequency, i is the imaginary number, k is the wave number, and H is the length of the structure, γ is the attenuation factor where $\gamma = \frac{1}{2Q}$ [40], S_1 and S_2 denote the spectrum of the two source terms and R_1 and R_2 are the reflection coefficients of the top and bottom reflectors, respectively. In the nominator, $e^{z(ik-\gamma|k|)}$ and $R_2 e^{(2H-z)(ik-\gamma|k|)}$ are the direct wave and the first reflection for S_1, while $e^{(H-z)(ik-\gamma|k|)}$ and $R_1 e^{(H+z)(ik-\gamma|k|)}$ are those for S_2. Their amplitudes are scaled by the attenuation terms that involve γ. The $R_1 R_2 e^{2H(ik-\gamma|k|)}$ term in the denominator is the common ratio in the power series representing higher-order reverberations between two reflectors. With Equation B1 and 1, the deconvolved wavefield using virtual source at z_a $(0 \le z_a \le H)$ can be written as:

$$D(z,z_a,\omega) = \frac{(e^{(z-z_a)(ik-\gamma|k|)} + R_2 e^{(2H-z-z_a)(ik-\gamma|k|)}) + \frac{S_2}{S_1}(e^{(H-z-z_a)(ik-\gamma|k|)} + R_1 e^{(H+z-z_a)(ik-\gamma|k|)})}{(1 + R_2 e^{2(H-z_a)(ik-\gamma|k|)}) + \frac{S_2}{S_1}(e^{(H-2z_a)(ik-\gamma|k|)} + R_1 e^{H(ik-\gamma|k|)})} \quad \text{(B2)}$$

$$= \frac{\frac{S_1}{S_2}(e^{(z+z_a-H)(ik-\gamma|k|)} + R_2 e^{(H-z+z_a)(ik-\gamma|k|)}) + (e^{(z_a-z)(ik-\gamma|k|)} + R_1 e^{(z_a+z)(ik-\gamma|k|)})}{\frac{S_1}{S_2}(e^{(H+2z_a)(ik-\gamma|k|)} + R_2 e^{H(ik-\gamma|k|)}) + (1 + R_1 e^{2z_a(ik-\gamma|k|)})}. \quad \text{(B3)}$$

When $|S_2|/|S_1| \approx 0$ in Equation B2, the deconvolved wavefield approaches the one source cases, same as the case when $|S_1|/|S_2| \approx 0$ in Equation B3. We observe the wavefield change when varying the relative intensity of the sources ($|S_1|/|S_2|$), correlation between sources (cc), reflection coefficients (R_1 and R_2), and adding additional sources in between, and then we compare the numerical results with the observed data (Figure 3). The default values are $|S_2|/|S_1| = 1$, $cc = 0.01$, $R_1 = R_2 = 0.5$ with $Q = 500$.

Appendix B.2 The effect of relative source intensity

We first vary $|S_1|/|S_2|$ from 0.1 to 10. In Figure B2b, when the intensity of the two source are comparable ($|S_1|/|S_2| = 1$), the relative amplitudes on the causal (positive lag-time) and acausal (negative lag-time) axes are comparable. The relative amplitude between the causal/acausal waves changes depending on the relative intensity of the

 doi:10.20944/preprints202105.0014.v1

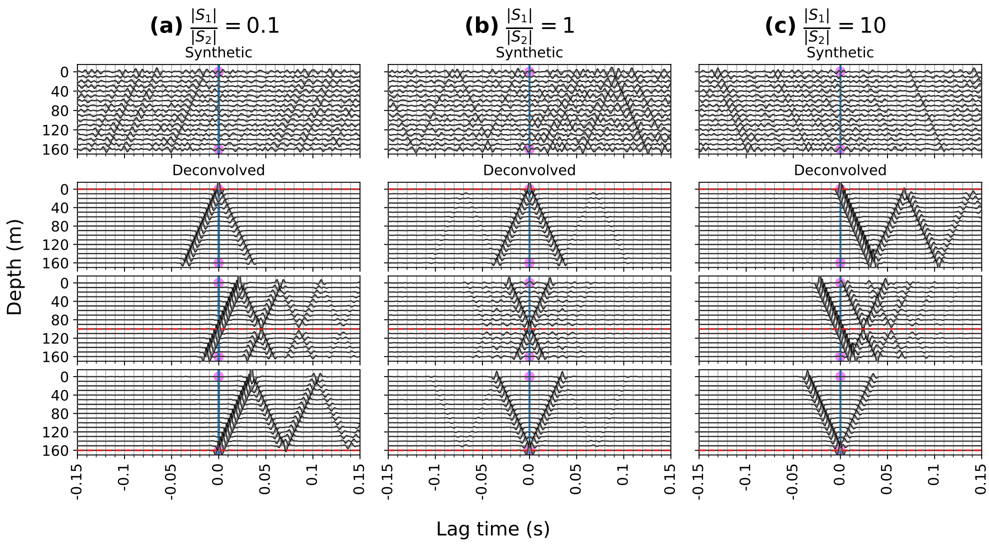

Figure B2. The synthetic and deconvolved wavefields for the two sources case with varying relative source intensity $|S_1|/|S_2|$: (**a**) $|S_1|/|S_2| = 0.1$, (**b**)$|S_1|/|S_2| = 1$, and (**c**) $|S_1|/|S_2| = 10$. The actual source locations are shown as the magenta balls in the synthetic wavefields. The virtual sources are shown as the red dashed lines in the deconvolved wavefields.

sources. In Figure B2a, when $|S_1| < |S_2|$, for channels above the virtual source (the red dashed lines), the waves at causal times have larger amplitude, whereas for channels below the virtual source, the waves at acausal times have larger amplitudes. Vice versa, in Figure B2c, the patterns reverse since $|S_1| > |S_2|$. To obtain similar results are the field data, where we have almost equivalent energy in the causal and acausal parts, we need to have two sources with about identical energy. Because the energy balance between the causal and acausal parts varies over the time (Figure 3), the location and/or intensity of the sources may change over the time. When one of the sources is dominant (Figure B2a,c), the deconvolved wavefields approach the single source cases. The time shift between multiples is the largest when the virtual source corresponds to the dominant real source. If we move the virtual source away from the dominant source, the multiples start to overlap; the farther away the virtual source is from the real source, the smaller the apparent time shift between the multiples.

Appendix B.3 The effect of source correlation

We vary the correlation coefficient between S_1 and S_2 from 0.01 (uncorrelated) to 0.99 (highly correlated). To generate synthetic data with certain degree of correlation, we first generate random, normalized data time-series and put them in rows to form matrix A. Then, we built a covariance matrix R with the desired correlation coefficient (cc) on the non-diagonals and 1s on the diagonals, and use the Cholesky decomposition to calculate matrix C such that $CC^T = R$. Multiplying A with C gives a new matrix where the cc between each row are as desired. Figure B3 shows the simulation results when the cc equals to 0.01, 0.5, and 0.99. When the two sources are not correlated (Figure B3a), only the virtual source emits waves. When the two sources are correlated (Figure B3b,c), the correlated source seems to emit another sets of waves in addition to that from the virtual source; the higher the correlation, the larger the amplitudes of those simultaneous direct waves. The waves emitted from the correlated source show symmetry on both causal and acausal axes.

Appendix B.4 The effect of reflection coefficients

Figure B4 shows the wavefields with variety of R_1 from 0.01, 0.5, to 0.99. When R_1 gets larger, for channels above the virtual source, the amplitudes of the acausal waves

Preprints (www.preprints.org) | NOT PEER-REVIEWED | Posted: 3 May 2021 doi:10.20944/preprints202105.0014.v1

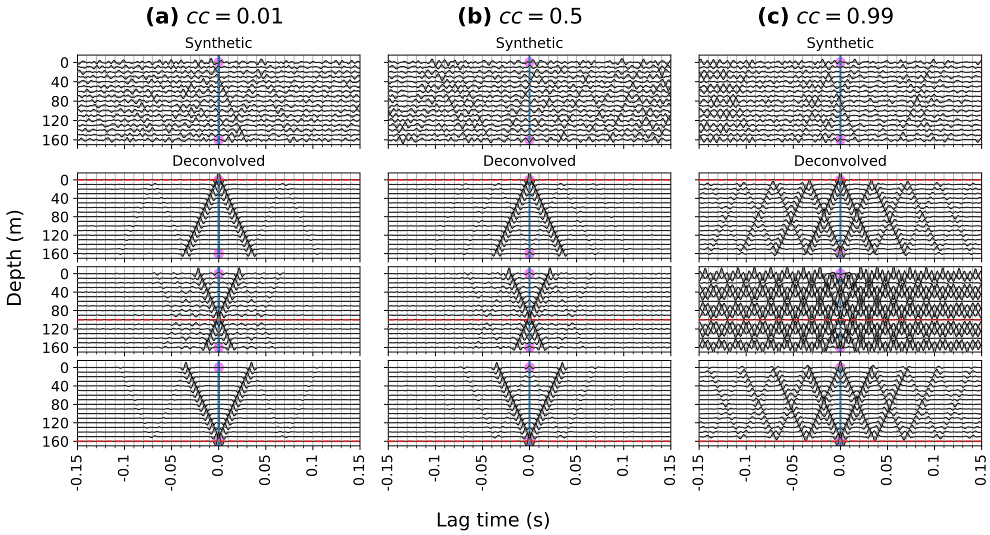

Figure B3. The synthetic and deconvolved wavefields for the case of two sources with varying degree of correlation between them: (**a**) not correlated ($cc = 0.01$), (**b**) partially correlated ($cc = 0.5$), and (**c**) highly correlated ($cc = 0.99$).

are enhanced; whereas for channels below the virtual source, the amplitudes of the causal waves are enhanced. This phenomenon of a larger R_1 is the opposite of the effect of larger S_1. Hence, the relative amplitudes between the causal and acausal axes can be affected by both the relative source intensity and the reflection coefficients.

Appendix B.5 The effect of adding more sources

We add an additional source in the middle of the string between S_1 and S_2 and make this added source either uncorrelated ($cc = 0.01$) or correlated ($cc = 0.7$) with S_1 (Figure B5). With the additional source, a "pseudo-reflector" at the depth corresponding to the middle source is created, and some energy of the incoming waves are reflected at this reflector. The pseudo-reflector is especially obvious when using the channel with the middle source to deconvolve (Figure B5 third from the top). However, using other non-source channels to deconvolve, the location of the third source becomes unclear due to overlapping of different waves (Figure B5 bottom). As similar to Figure B3, the correlation between physical sources make the deconvolved wavefields complicated because of the crosstalk between these sources (Figure B5). The symmetries shown in Figure B5 are consistent with the results in Nakata and Snieder [31] when placing random distributed sources along the structure. Although, their results do not have clear pseudo-reflectors due to the fact that many sources are in the system.

Preprints (www.preprints.org) | NOT PEER-REVIEWED | Posted: 3 May 2021 doi:10.20944/preprints202105.0014.v1

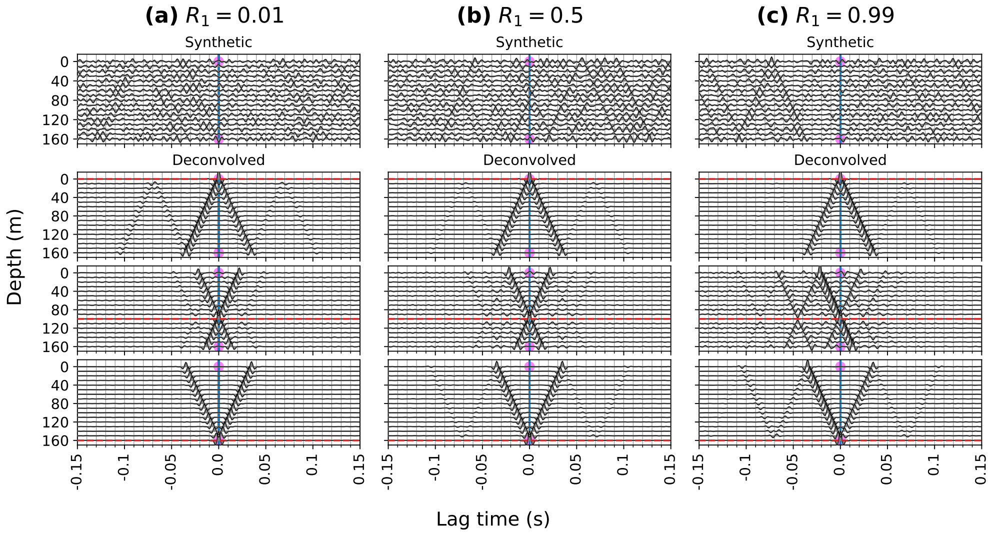

Figure B4. The synthetic and deconvolved wavefields for the two sources case with varying reflection coefficient of the top reflector R_1: (**a**) low reflectivity ($R_1 = 0.01$), (**b**) intermediate reflectivity ($R_1 = 0.5$), and (**c**) high reflectivity ($R_1 = 0.99$).

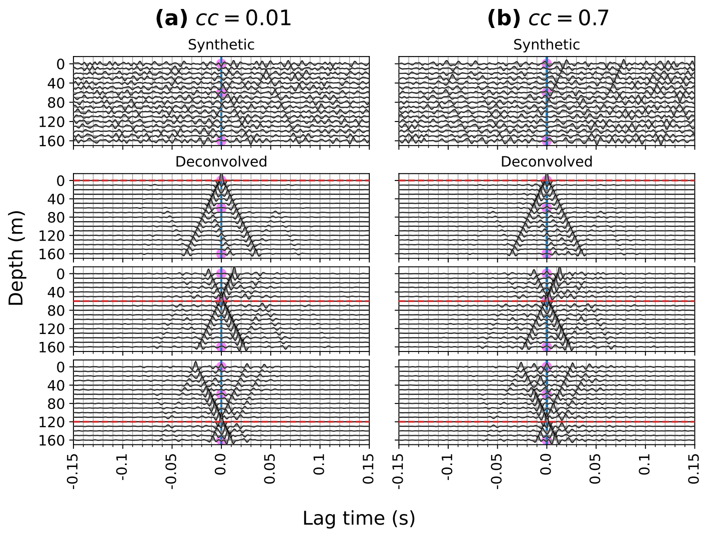

Figure B5. The synthetic and deconvolved wavefields when adding a source in the middle between the top (S_1) and the bottom (S_2) sources. (**a**) The middle source and S_1 are uncorrelated ($cc = 0.01$). (**b**) The middle source and S_1 are partially correlated ($cc = 0.7$). In both cases, S_1 and S_2 are uncorrelated.

References

1. Johannessen, K.; Drakeley, B.K.; Farhadiroushan, M.; others. Distributed Acoustic Sensing-a new way of listening to your well/reservoir. SPE Intelligent Energy International. Society of Petroleum Engineers, 2012.
2. Finfer, D.C.; Mahue, V.; Shatalin, S.; Parker, T.; Farhadiroushan, M.; others. Borehole Flow Monitoring using a Non-intrusive Passive Distributed Acoustic Sensing (DAS). SPE Annual Technical Conference and Exhibition. Society of Petroleum Engineers, 2014.
3. Naldrett, G.; Cerrahoglu, C.; Mahue, V.; others. Production monitoring using next-generation distributed sensing systems. *Petrophysics* **2018**, *59*, 496–510.
4. Dickenson, P. ESP Monitoring using Heterodyne Distributed Vibration Sensor (hDVS). European Artificial Lift Forum, 2014.
5. Mateeva, A.; Lopez, J.; Potters, H.; Mestayer, J.; Cox, B.; Kiyashchenko, D.; Wills, P.; Grandi, S.; Hornman, K.; Kuvshinov, B.; others. Distributed acoustic sensing for reservoir monitoring with vertical seismic profiling. *Geophysical Prospecting* **2014**, *62*, 679–692.
6. Daley, T.; Miller, D.; Dodds, K.; Cook, P.; Freifeld, B. Field testing of modular borehole monitoring with simultaneous distributed acoustic sensing and geophone vertical seismic profiles at Citronelle, Alabama. *Geophysical Prospecting* **2016**, *64*, 1318–1334.
7. Byerley, G.; Monk, D.; Aaron, P.; Yates, M. Time-lapse seismic monitoring of individual hydraulic frac stages using a downhole DAS array. *The Leading Edge* **2018**, *37*, 802–810.
8. Correa, J.; Pevzner, R.; Bona, A.; Tertyshnikov, K.; Freifeld, B.; Robertson, M.; Daley, T. 3D vertical seismic profile acquired with distributed acoustic sensing on tubing installation: A case study from the CO2CRC Otway Project. *Interpretation* **2019**, *7*, SA11–SA19.
9. Webster, P.; Wall, J.; Perkins, C.; Molenaar, M. Micro-seismic detection using distributed acoustic sensing. In *SEG Technical Program Expanded Abstracts 2013*; Society of Exploration Geophysicists, 2013; pp. 2459–2463.
10. Ghahfarokhi, P.K.; Wilson, T.H.; Carr, T.R.; Kumar, A.; Hammack, R.; Di, H. Integrating distributed acoustic sensing, borehole 3C geophone array, and surface seismic array data to identify long-period long-duration seismic events during stimulation of a Marcellus Shale gas reservoir. *Interpretation* **2019**, *7*, SA1–SA10.
11. Hartog, A.H. *An introduction to distributed optical fibre sensors*; CRC press, 2017.
12. Bruno, M.S.; Lao, K.; Oliver, N.; Becker, M. Use of Fiber Optic Distributed Acoustic Sensing for Measuring Hydraulic Connectivity for Geothermal Applications. Technical report, GeoMechanics Technologies, Monrovia, CA (United States), 2018.
13. Munn, J.D.; Coleman, T.I.; Parker, B.L.; Mondanos, M.J.; Chalari, A. Novel cable coupling technique for improved shallow distributed acoustic sensor VSPs. *Journal of Applied Geophysics* **2017**, *138*, 72–79.
14. Zhan, Z. Distributed acoustic sensing turns fiber-optic cables into sensitive seismic antennas. *Seismological Research Letters* **2020**, *91*, 1–15.
15. Feigl, K.L.; Team, P. Overview and preliminary results from the PoroTomo project at Brady Hot Springs, Nevada: Poroelastic tomography by adjoint inverse modeling of data from seismology, geodesy, and hydrology. 42nd Workshop on Geothermal Reservoir Engineering. Stanford University Stanford, CA, 2017, pp. 1–15.
16. Feigl, K.L.; Parker, L.M. PoroTomo Final Technical Report: Poroelastic Tomography by Adjoint Inverse Modeling of Data from Seismology, Geodesy, and Hydrology. Technical report, Univ. of Wisconsin, Madison, WI (United States), 2019.
17. Patterson, J.R.; Cardiff, M.; Coleman, T.; Wang, H.; Feigl, K.L.; Akerley, J.; Spielman, P. Geothermal reservoir characterization using distributed temperature sensing at Brady Geothermal Field, Nevada. *The Leading Edge* **2017**, *36*, 1024a1–1024a7.
18. Patterson, J.R. Understanding constraints on geothermal sustainability through reservoir characterization at Brady Geothermal Field, Nevada. PhD thesis, University of Wisconsin–Madison, 2018.
19. Miller, D.E.; Coleman, T.; ZENG, X.; PATTERSON, J.R.; REINISCH, E.C.; CARDIFF, M.A.; WANG, H.F.; FRATTA, D.; TRAINOR-GUITTON, W.; THURBER, C.H. DAS and DTS at Brady Hot Springs: observations about coupling and coupled interpretations. Proceedings of the 43rd Workshop on Geothermal Reservoir Engineering, Stanford, CA, USA, 2018, pp. 12–14.
20. Trainor-Guitton, W.; Guitton, A.; Jreij, S.; Powers, H.; Sullivan, B. 3D Imaging of Geothermal Faults from a Vertical DAS Fiber at Brady Hot Spring, NV USA. *Energies* **2019**, *12*, 1401.
21. Nakata, N.; Snieder, R. Estimating near-surface shear wave velocities in Japan by applying seismic interferometry to KiK-net data. *Journal of Geophysical Research: Solid Earth* **2012**, *117*.
22. Sawazaki, K.; Sato, H.; Nakahara, H.; Nishimura, T. Time-lapse changes of seismic velocity in the shallow ground caused by strong ground motion shock of the 2000 Western-Tottori earthquake, Japan, as revealed from coda deconvolution analysis. *Bulletin of the Seismological Society of America* **2009**, *99*, 352–366.
23. Yamada, M.; Mori, J.; Ohmi, S. Temporal changes of subsurface velocities during strong shaking as seen from seismic interferometry. *Journal of Geophysical Research: Solid Earth* **2010**, *115*.
24. Bonilla, L.F.; Guéguen, P.; Ben-Zion, Y. Monitoring coseismic temporal changes of shallow material during strong ground motion with interferometry and autocorrelation. *Bulletin of the Seismological Society of America* **2019**, *109*, 187–198.
25. Snieder, R.; Safak, E. Extracting the building response using seismic interferometry: Theory and application to the Millikan Library in Pasadena, California. *Bulletin of the Seismological Society of America* **2006**, *96*, 586–598.
26. Nakata, N.; Snieder, R.; Kuroda, S.; Ito, S.; Aizawa, T.; Kunimi, T. Monitoring a building using deconvolution interferometry. I: Earthquake-data analysis. *Bulletin of the Seismological Society of America* **2013**, *103*, 1662–1678.
27. Tonegawa, T.; Nishida, K.; Watanabe, T.; Shiomi, K. Seismic interferometry of teleseicmic S-wave coda for retrieval of body waves: an application to the Philippine Sea slab underneath the Japanese Islands. *Geophysical Journal International* **2009**, *178*, 1574–1586.

28. Cardiff, M.; Lim, D.D.; Patterson, J.R.; Akerley, J.; Spielman, P.; Lopeman, J.; Walsh, P.; Singh, A.; Foxall, W.; Wang, H.F.; others. Geothermal production and reduced seismicity: Correlation and proposed mechanism. *Earth and Planetary Science Letters* **2018**, *482*, 470–477.
29. Wapenaar, K.; Draganov, D.; Snieder, R.; Campman, X.; Verdel, A. Tutorial on seismic interferometry: Part 1—Basic principles and applications. *Geophysics* **2010**, *75*, 75A195–75A209.
30. Seats, K.J.; Lawrence, J.F.; Prieto, G.A. Improved ambient noise correlation functions using Welch's method. *Geophysical Journal International* **2012**, *188*, 513–523.
31. Nakata, N.; Snieder, R. Monitoring a building using deconvolution interferometry. II: Ambient-vibration analysis. *Bulletin of the Seismological Society of America* **2014**, *104*, 204–213.
32. Ellis, D.V.; Singer, J.M. *Well logging for earth scientists*; Vol. 692, Springer, 2007.
33. Haynes, W.M. *CRC handbook of chemistry and physics*; CRC press, 2014.
34. Parker, L.; Thurber, C.; Zeng, X.; Li, P.; Lord, N.; Fratta, D.; Wang, H.; Robertson, M.; Thomas, A.; Karplus, M.; others. Active-source seismic tomography at the Brady Geothermal Field, Nevada, with dense nodal and fiber-optic seismic arrays. *Seismological Research Letters* **2018**, *89*, 1629–1640.
35. Thurber, C.H.; Parker, L.; Li, P.; Fratta, D.; Zeng, X.; Feigl, K.L.; Ak, E.; Lord, N. Active-Source Seismic Tomography at Bradys Geothermal Field, Nevada, with Dense Nodal and Fiber-Optic Seismic Arrays. AGU Fall Meeting Abstracts, 2017, Vol. 2017, pp. S32A–04.
36. Rama Rao, V.; Vandiver, J. Acoustics of fluid-filled boreholes with pipe: Guided propagation and radiation. *The Journal of the Acoustical Society of America* **1999**, *105*, 3057–3066.
37. Mott, G. Temperature dependence of ultrasonic parameters. *Review of progress in quantitative nondestructive evaluation.* **1984**, *3*, 1137–1148.
38. Droney, B.; Mauer, F.; Norton, S.; Wadley, H.N. Ultrasonic Sensors to Measure Internal Temperature Distribution. In *Review of Progress in Quantitative Nondestructive Evaluation*; Springer-Verlag US, 1986; Vol. 5A, chapter Chapter 3: Sensors and Signal Processing, pp. 643–650.
39. Siler, D.L.; Faulds, J.E. Three-dimensional geothermal fairway mapping: examples from the western Great Basin, USA. Technical report, Geothermal Resources Council, Davis, CA (United States), 2013.
40. Aki, K.; Richards, P.G. *Quantitative seismology*; University Science Books, 2002.